

SPECTROSCOPY OF SOLAR PROMINENCES SIMULTANEOUSLY FROM SPACE AND GROUND

G. Stellmacher¹, E. Wiehr² and I. E.
Dammasch³

© Springer

Abstract We present a comprehensive set of spectral data from two quiescent solar prominences observed in parallel from space and ground: with the VTT, simultaneous two-dimensional imaging of $H\beta$ 4862 Å and Ca II 8542 Å yields a constant ratio, indicating small spatial pressure variations over the prominence. With the Gregory, simultaneous spectra of Ca II 8542 Å and He I 10830 Å were taken, their widths yielding $8000 < T_{kin} < 9000$ K and $v_{nth} < 8$ km/s. The intensity ratio of the helium triplet components gives an optical thickness of $\tau < 1.0$ for the fainter and $\tau \leq 2.0$ for the brighter prominence. The τ_0 values allow to deduce the source function for the central line intensities and thus the relative population of the helium ³S and ³P levels with a mean excitation temperature $T_{ex}^{mean} = 3750$ K.

With SUMER, we sequentially observed 6 spectral windows containing higher Lyman lines, 'cool' emission lines from neutrals and singly charged atoms, as well as 'hot' emission lines from ions like O IV, O V, N V, S V and S VI. The EUV lines show pronounced maxima in the main prominence body as well as 'side-locations' where the 'hot' lines are enhanced with respect to the 'cool' lines. The line radiance of 'hot' lines blue-wards of the Lyman series limit ($\lambda < 912$ Å) appear reduced in the main prominence body. This absorption is also visible in TRACE images of Fe IX/x 171 Å as fine dark structure which covers only parts of the main ('cool') prominence body.

The Lyman lines show a smooth decrease of line widths and radiance with increasing upper level $k = 5$ through 19. For $5 \leq k \leq 8$ the level population follows a Boltzmann distribution with $T_{ex} > 6 \cdot 10^4$ K; higher levels $k > 8$ appear more and more overpopulated. The larger widths of the Lyman lines require high non-thermal broadening close to that of 'hot' EUV lines. In contrast, the He II emission is more related to the 'cool' lines.

Keywords: Prominences, Quiescent, EUV emission

¹ Institute d'Astrophysique, Paris, France, email: stell@iap.fr

² Institut für Astrophysik, Göttingen, Germany, email:
ewiehr@astro.physik.uni-goettingen.de

³ Max-Planck-Institut für Aeronomie, Katlenburg-Lindau,
Germany,

1. Introduction

Solar prominences are spectacular manifestations of NLTE plasma emissions from atoms and ions coexisting in very different excitation states. Lines from neutral metals and their singly charged ions indicate a cool plasma component, whereas lines from higher charged ions such as O IV, O V, N V, S VI and S V indicate a much hotter component. The spatial distribution of cold and hot plasma and its relation to the fine-structure ('threads', visible, e.g., in H α images) is an essential problem in prominence physics. The line shifts from bulk velocities show a good coherence over wide spatial scales largely independent of the line formation temperature. In contrast, the integrated line intensities show a good spatial correlation only for lines from atoms with similar ionization states.

Two opposed scenarios have been proposed to explain the distribution of cool and hot plasma in prominences: (i) cold threads, each surrounded by a hot transition layer where the observed EUV emissions originate or (ii) isothermal threads of different temperatures whose relative number may vary. The second view might be favored by the observations from UV rocket spectra of the eclipsed sun by Yang, Nicholls, and Morgan (1975), who found the prominence sizes to increase with temperature. Similarly, HRTS data from Wijk, Dere and Schmieder (1993) and SUMER data from de Boer, Stellmacher and Wiehr (1998) indicate that the lines from higher ionized atoms are preferentially visible in peripheral prominence parts.

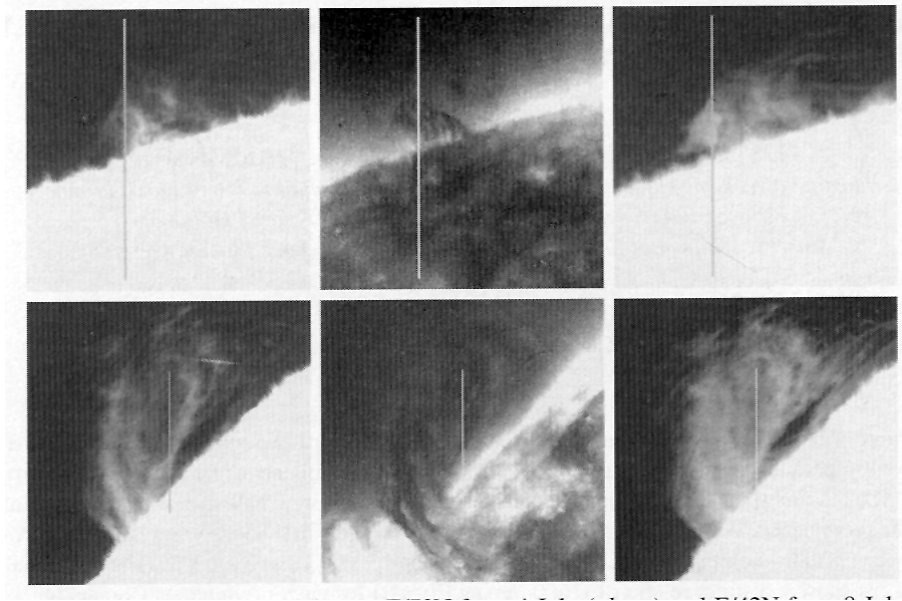


Figure 1. TRACE images of prominence E/70N from 4 July (*above*) and E/42N from 8 July 2000 (*lower panel*) in the 1600 Å continuum window (*left*), in the coronal Fe IX/X 171 Å line showing absorption in the cool, dense prominence core (*middle*), and in the Ly α line (*right panel*); the 120'' long SUMER slit is indicated.

Observations in the visible spectral region mainly provide information about the cool parts, whereas EUV spectra particularly reflect emissions from hotter parts of a prominence. We present coordinated spectroscopic prominence observations from the ground, using at Tenerife the VTT and the GCT; in parallel we took EUV spectra from space with SUMER on board SOHO and two-dimensional images with TRACE. We observed two prominences at the east limb, one 'polar crown type' at 70° N on 4 July 2000, and another at lower latitude 42° N on 8 July 2000 (hereafter referred to as E/70N and E/42N).

2. Ground-Based observations

With the Vacuum Tower Telescope (VTT) on Tenerife two-dimensional images were taken simultaneously through narrow-band filters covering the integrated emissions of $H\beta$ 4862 Å and of Ca II 8542 Å. The pressure-sensitive ratio of both lines is in agreement with our former observations (Stellmacher & Wiehr 2000). Comparison with model calculations by Gouttebroze and Heinzel (2002) for the optically thin case $\tau(H\beta) \leq 1.0$ (which is generally valid for quiescent prominences) shows that our data is compatible with a gas-pressure of $0.1 < P_g < 1.0 \text{ dyn/cm}^2$.

In parallel we observed with the Gregory-Coude Telescope (GCT) on Tenerife spectra of the near infrared lines Ca II 8542 Å and He I 10830 Å (hereafter referred to as Ca IR and He IR) simultaneously in the 5th and the 4th grating order of the spectrograph. The good spectral and spatial coherence of Ca IR and He IR, mainly visible in the similar shifts from bulk velocities (Fig. 2), indicates a common emitting volume.

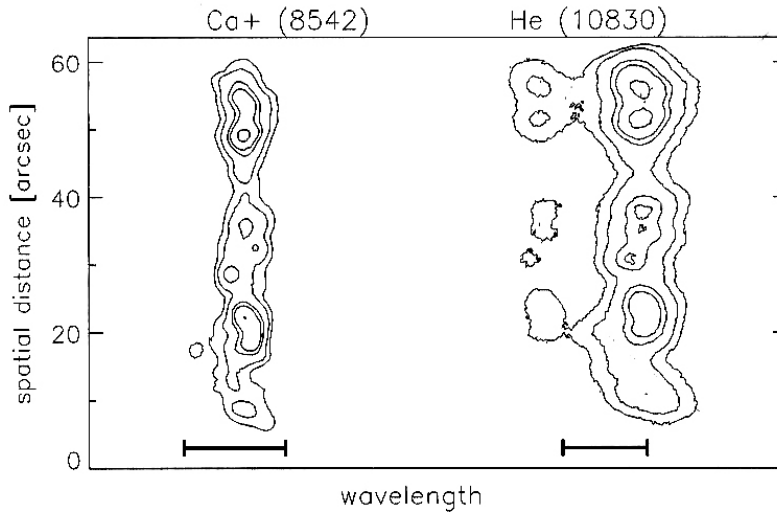


Figure 2. Iso-contours of the simultaneously observed emission lines Ca II 8542 Å (left side) and He I 10830 Å with the well separated blue triplet component in prominence E/70N; the bars give 1 Å; λ increasing to the right

2.1. The Ca II 8542 emission

The widths of the Ca IR line can be considered as purely Doppler broadened: due to the large atomic mass almost entirely by non-thermal (Maxwellian) velocities. For optically thin layers, the integrated emission ('line radiance') is proportional to the central line intensity: $E = \sqrt{\pi} \cdot \Delta\lambda_D \cdot I_0$. The lower limit of the E versus I_0 relation yields minimum Doppler-widths $\Delta\lambda_D = 120 \text{ m}\text{\AA}$ and $130 \text{ m}\text{\AA}$ for prominences E/70N and E/42N, respectively. The observed emission relation (Fig. 3) shows that each prominence is characterized by a well-defined relation; for the fainter prominence E/70N the slope is steeper than for the brighter one E/42N ('branching', cf., Engvold, 1978; Stellmacher and Wiehr, 1995).

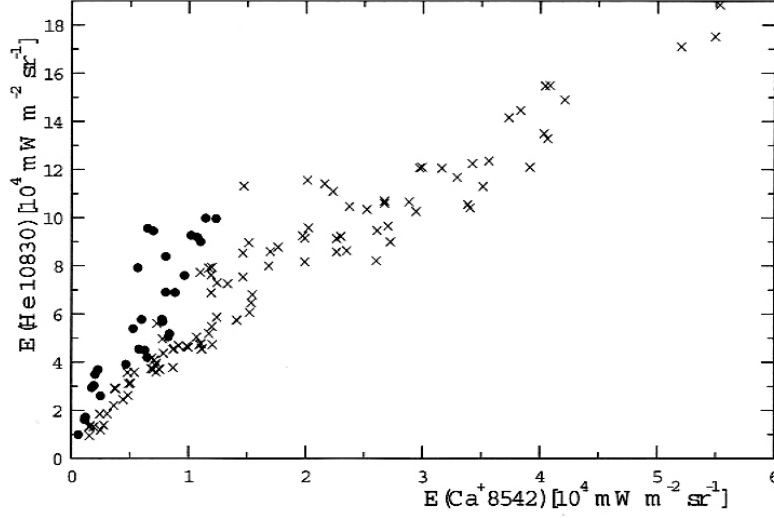


Figure 3. Observed emission relations of He I 10830 Å versus Ca II 8542 Å for prominences E/70N (dots) and E/42N (crosses).

2.2. The helium triplet

The He I 10830 Å line triplet is composed of a blue component at 10829.08 Å ($^3P_o - ^3S_1$) and two red components at 10830.25 Å ($^3P_1 - ^3S_1$) and at 10830.34 Å ($^3P_2 - ^3S_1$). They allow a simple evaluation of the total optical thickness, which is described in more detail in the original version (Solar Phys. 217, 133) of this paper. Since the Doppler width exceeds the 90 Å (fine-structure) separation of the two red components, these two lines form an unresolved broader line; the blue component, however, is well separated (cf., Fig. 2). The ratio between the central line intensities of the combined (two) red and the faint (isolated) blue component, I_0^{red}/I_0^{blue} is now calculated as a function of τ_0 , the optical thickness at the center of the strongest (red) triplet component; (the dependence on the width $\Delta\lambda_D$ is found to be negligible).

For very small τ_0 a ratio of 8:1 is obtained, which corresponds to the relative values of the absorption oscillator strengths, f_{ik} . Increasing τ_0 saturates the combined red components, while the blue component still grows, yielding a ratio of 3 : 1 for $\tau_0 = 2.0$. This calculated relation now allows us to deduce τ_0 from the ratio of the line-center intensities I_0^{red}/I_0^{blue} , observed at a given prominence location. We can then relate the line radiance of the complete HeIR triplet with the total optical thickness of the two (unresolved) red components and find that prominence E/70N has maximum values of $\tau^{red} = 1.0$, whereas prominence E/42N reaches $\tau^{red} = 2.0$.

2.3. Line widths

Our profile calculations allow us to convert the observed line widths of the superposed two red components into true Doppler widths, $\Delta\lambda_D$, for which we find almost identical values as from the isolated (and optically thin) blue component. These widths show a close relation with the CaIR widths (Fig. 4), as to be expected from the good coherence of the HeIR and CaIR lines (Fig. 2).

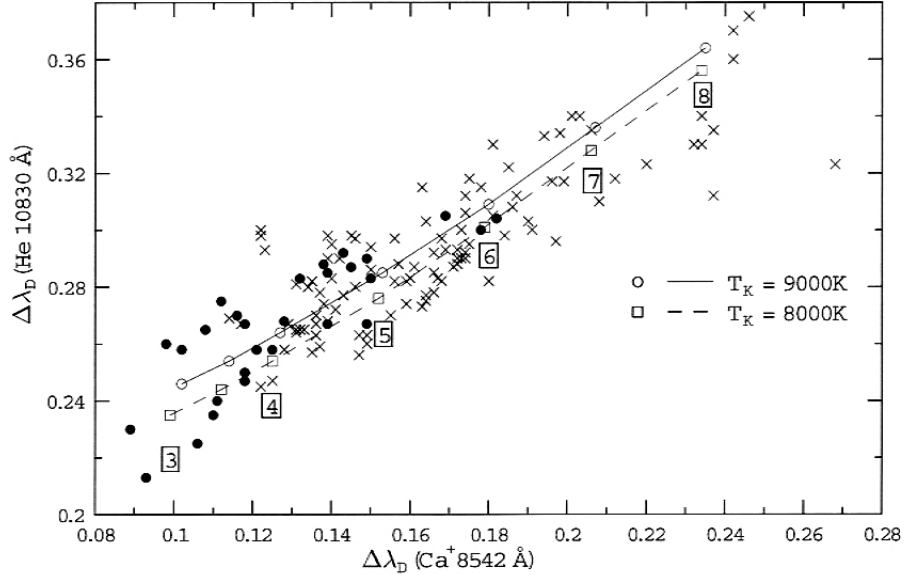


Figure 4. Deduced dependence of the line emissions E(He I 10830 Å) on $\tau^{red}(= 1.56\tau_0)$ for the prominences E/70N (dots) and E/42N (crosses).

We superpose in Figure 4 calculated Doppler widths, which show that the fainter prominence (E/70N) is characterized by $8000 < T_{kin} < 9500$ K the brighter one (E/42N) being slightly cooler with $7500 < T_{kin} < 9000$ K. This confirms earlier results by Stellmacher and Wiehr (1994, 1995) who found brighter prominences to be cooler (and less structured).

The non-thermal velocities amount to $3 < v_{nth} < 6$ km/s and $4 < v_{nth} < 8$ km/s for E/70N and E/42N, respectively. This agrees with the Doppler widths of $\Delta\lambda_D$ (Ca IR) = 120 mÅ and 130 mÅ, respectively, obtained from the E versus I_0 relation (Sec. 2.1). Assuming purely non-thermal broadening, this corresponds to 4.2 km/s and 4.5 km/s for E/70N and E/42N, respectively. Hence, the fainter prominence shows higher T_{kin} but smaller v_{nth} than the brighter one.

3. Space Observations

In parallel with these ground-based observations, we took EUV spectra with SUMER on board SOHO sequentially for the ranges 910-955, 1060-1100, 1225-1270, 1245-1295, 1295-1340, and 1540-1580 Å. The total exposure time for each spectrum was 120 s; the complete series of the six spectra was repeated 15 times over four hours. A slit of 1 arcsec width and 120 arcsec length was oriented along the solar north-south direction. The stray-light was taken from a sequence taken on 10 July where the SUMER slit did not cover a prominence; it was subtracted after careful alignment of the limb positions.

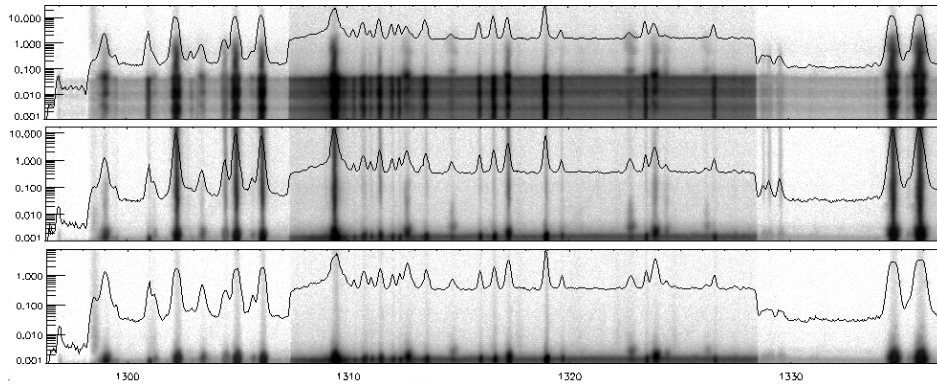


Figure 5. SUMER spectra in the range 1295-1340 Å (first order) and 648-670 Å (second order) for the prominences E/70N (*upper*), E/42N (*middle*) and a region without prominence emission, taken for the background intensities (*bottom*); the solar disk appears dark in the lower parts of the spectra.

As an example of the SUMER spectra we show in Figure 5 the range 1295-1340 Å for both prominences in comparison to an off-limb region without prominence. It can be seen that ions of different formation temperature preferentially emit in different parts of the prominences.

3.1. The Lyman lines

Among our large sample of EUV emissions, the Lyman lines are of particular interest. Since damping does not play a significant role in prominences, the emission lines can be fitted by Gaussian profiles in the wings. Figure 6 shows observed Lyman lines together with their respective fits. The lines are noticeably

reversed for upper levels $5 \leq k \leq 7$ and still saturated for $8 \leq k \leq 9$. For these lines, the cores are kept as measured and only the wings are assumed Gaussian. For the higher Lyman members $10 \leq k \leq 19$, the whole profiles are represented by Gaussians considering spectral line superpositions.

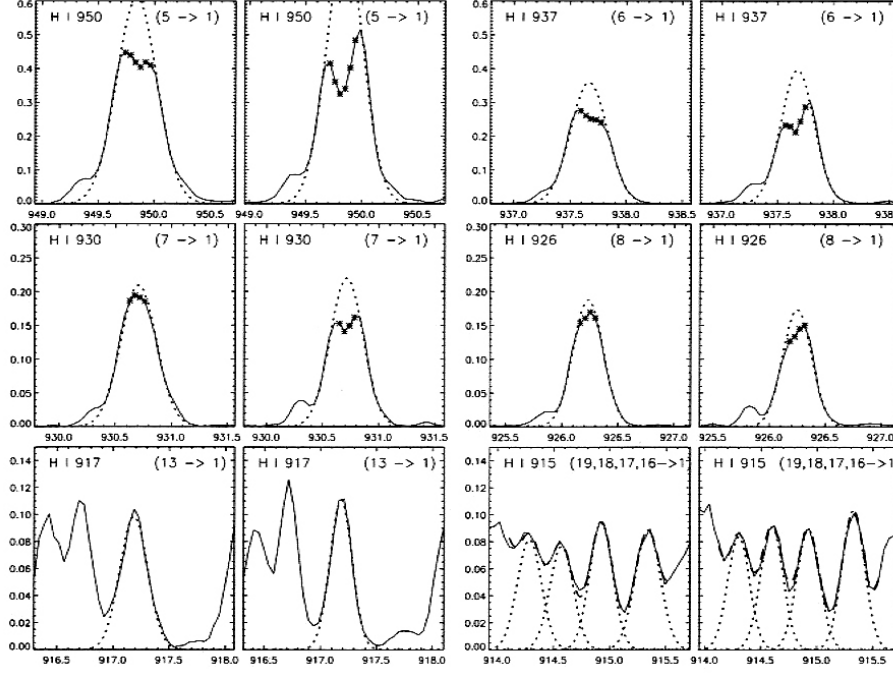


Figure 6. Observed Lyman line profiles with upper levels $k = 5, 6, 7, 8, 13$, and $16 \dots 19$; for prominence E/70N (*left*), prominence E/42N (*right side*); Gaussian fits for $k < 10$ only to the wings, the cores are taken from raw data (*asterisks*); for $16 \leq k \leq 19$ the superposed Gaussians (*dashes*) deviate from the observed spectrum (*full line*) by typically 0.005...0.011.

Our fits assure a highly accurate representation of the Lyman profiles and allow a reliable determination of their relative widths, $\Delta\lambda_e/\lambda$, and their line radiances (i.e., free from blends, mainly the He II lines). The thus obtained widths are plotted in Figure 7 versus $\log(\lambda f_{1,k})$ (being proportional to $\log \tau_{1,k}$). Prominence E/42N exhibits narrower lines than prominence E/70N - in agreement with the ground-based results (Fig. 4). Both curves are nearly parallel and decrease smoothly with increasing k and thus with decreasing optical thickness $\tau_{1,k}$. Even the smallest widths $\Delta\lambda_e/\lambda = 14 \cdot 10^{-5}$ largely exceed $\Delta\lambda_D/\lambda = 4.3 \cdot 10^{-5}$ expected for Balmer lines with the T_{kin} and v_{nth} from our ground based spectra. The large widths of the Lyman lines can not arise from Stark broadening since we consider only upper levels $k < 20$ (Hirayama, 1971). Instead, they indicate an origin from hotter layers of the prominence-corona transition region, PCTR.

The integrated line intensity ('radiance') versus $\log(\lambda f_{1,k})$, shows a well defined relation ('curve-of-growth') indicating a common state of excitation. From the Lyman radiance, $E_{1,k}$, level populations along the line of sight, $\log(n/g_k) \cdot d$, may be obtained following the relation for optically thin emissions: $\log(n_k/g_k) = \log((E_{1,k}\lambda_{1,k})/(A_{1,k}g_{1,k}))$

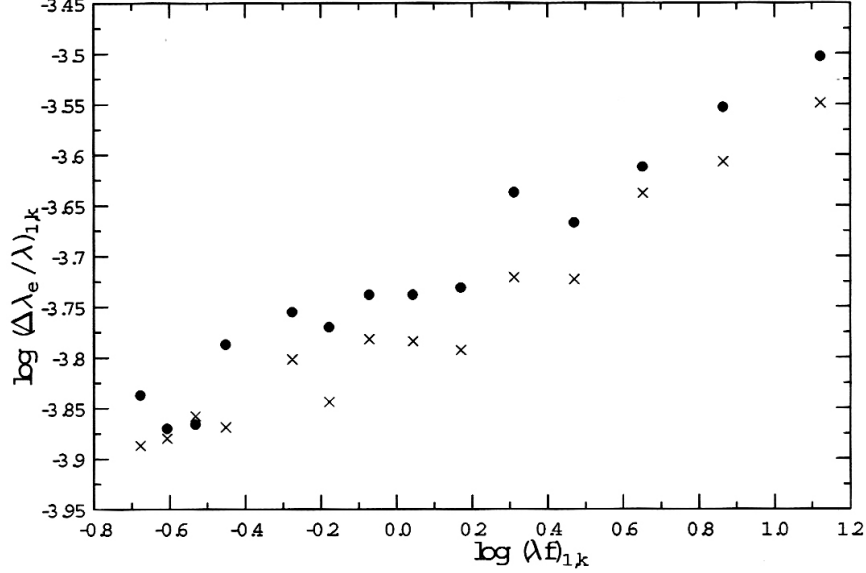


Figure 7. Averaged line widths at 1/e intensity as a function of the oscillator strength f for the Lyman members with upper levels $19 > k > 5$ (from left to right: $k = 15$ omitted) for prominences E/70N (dots) and E/42N (crosses).

Plotting these values versus the corresponding energy distance from the ionization limit $\Delta\chi = (\chi_\infty - \chi_k) = (13.6 \text{ eV} - \chi_k)$ shows a smooth Boltzmann distribution for the strongly saturated lines (with pronounced central reversal) up to level $k = 8$, which could be described by an equivalent excitation temperature of $T_{ex} > 6 \cdot 10^4 \text{ K}$. The higher levels, $k > 9$ with $\Delta\chi < 0.2 \text{ eV}$ (i.e., virtually the same) appear more and more overpopulated. Such a behavior can also be extracted from the data of Heinzel et al. (2001, cf., their Table 4).

3.2. Spatial distribution of the EUV line intensities

In agreement with our former study (deBoer, Stellmacher, and Wiehr, 1998), we find in the present data a good spatial coherence of such emissions which correspond to similar ionization states, respectively formation temperatures. For both prominences, the intensity scans along the slit in Figures 8 and 9 show local enhancements of the 'hotter' lines (S IV, S V, O V; at 38" in E/70N and at 28" in E/42N) which are hardly seen in the 'cooler' lines (N I, C I, Fe II and Ni II).

Concerning the He II lines, we find that the spatial distribution of their emission is rather related to that of 'cool' lines as, e.g., Fe II 1563 Å. Interestingly, the Lyman lines show a similar spatial variation (in Figures 8 and 9, Ly-10 is given as an example) and do not noticeably weaken at locations where lines from highly charged ions are strengthened. Since these regions can be considered to be preferentially composed of hot temperature plasma, their Lyman emissions will mainly reflect a recombination equilibrium. This might explain the small dependence of the intensity on k for higher Lyman members.

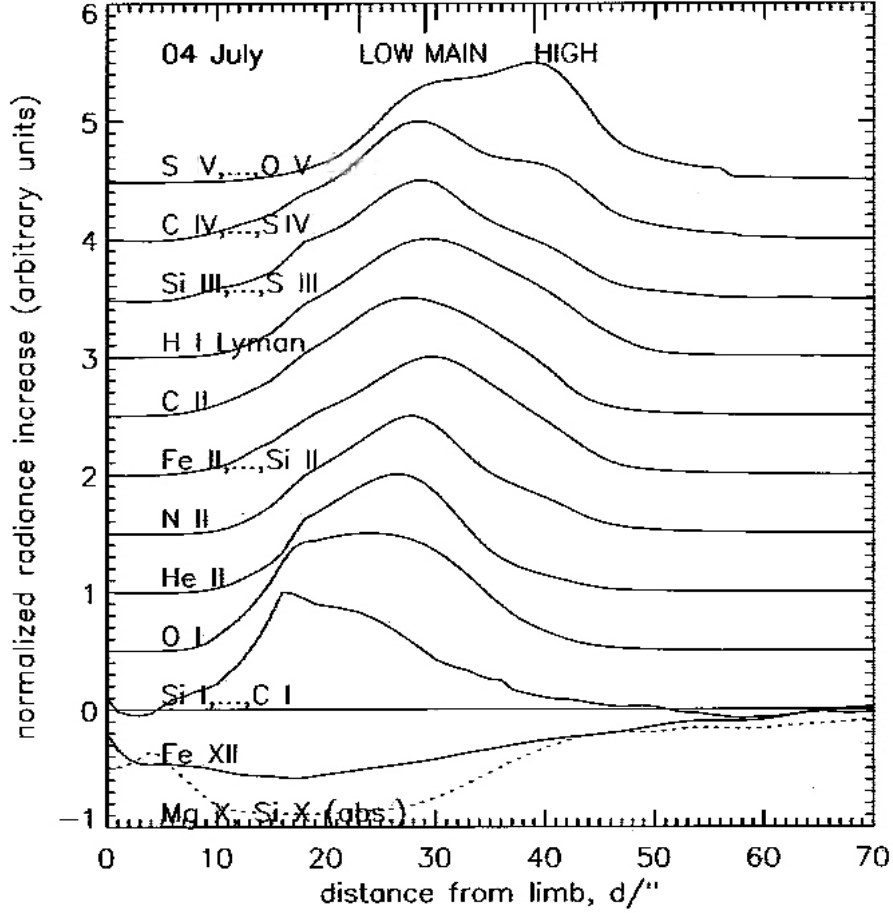


Figure 8. Spatial variation (along the SUMER slit) of the EUV emissions in prominence E/70N; counts integrated over the respective lines, arranged for increasing formation temperature (*upwards*); negative values indicate absorbed coronal lines; the Lyman lines are represented by $k = 10$. The 7'' regions selected for spatial averaging are indicated at the *top* of the Figure.

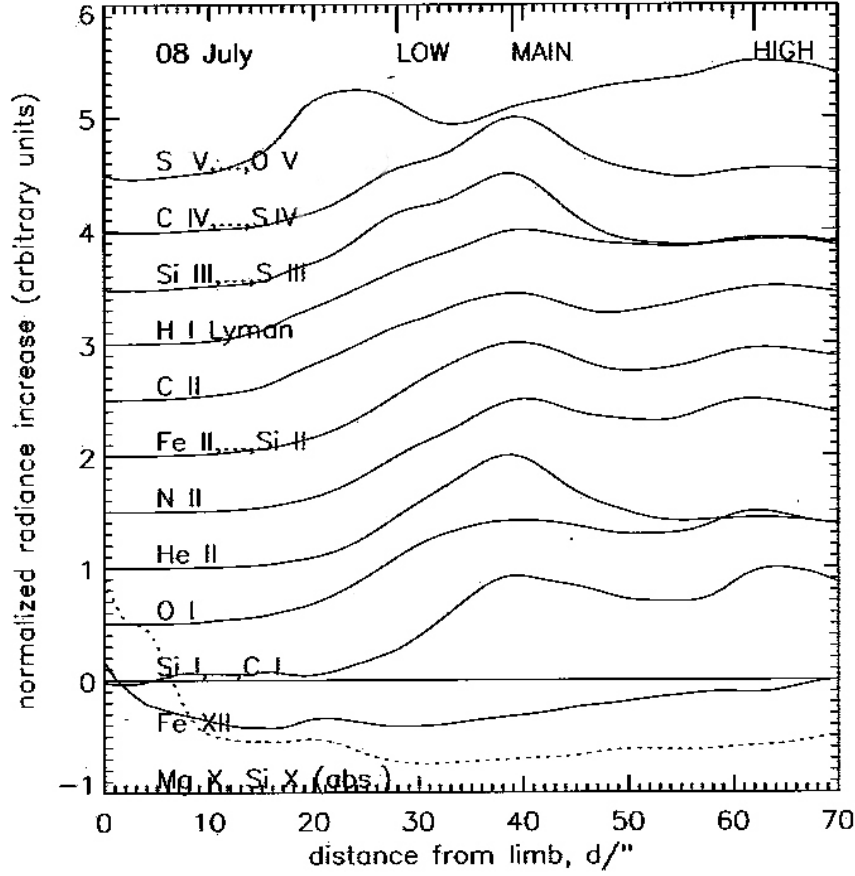


Figure 9. Same as Figure 8 but for prominence E/42N.

3.3. 'Absorbed' EUV lines

The purely coronal EUV lines (e.g., Fe XII 1242 Å; cf., lowest curves in Figures 8 and 9) show an 'absorption' in the sense of reduced radiance as compared to that from corresponding locations above the limb free from prominences. For coronal lines $\lambda < 912$ Å, i.e. blue-ward of the Lyman series limit (e.g., Mg X 625 Å), an additional absorption occurs. Both cases can be seen in Figures 8 and 9 at locations of maximum emission of the 'chromospheric' lines (e.g., Si I, C I). This relation of the EUV absorption to cool (dense) prominence matter is nicely seen comparing the Fe IX/x 171 Å image with the $L\alpha$ image from TRACE (Fig. 1) and with the $H\alpha$ image from VTT. In Figure 10 we give the profiles of the two 'coronal' lines Fe XII 1242 Å ($\lambda > 912$ Å), and Mg X 625 Å ($\lambda < 912$ Å) in comparison with corresponding profiles from prominence-free locations at equal height above the solar limb. The additional absorption by the Lyman continuum is well visible for Mg X 625 Å.

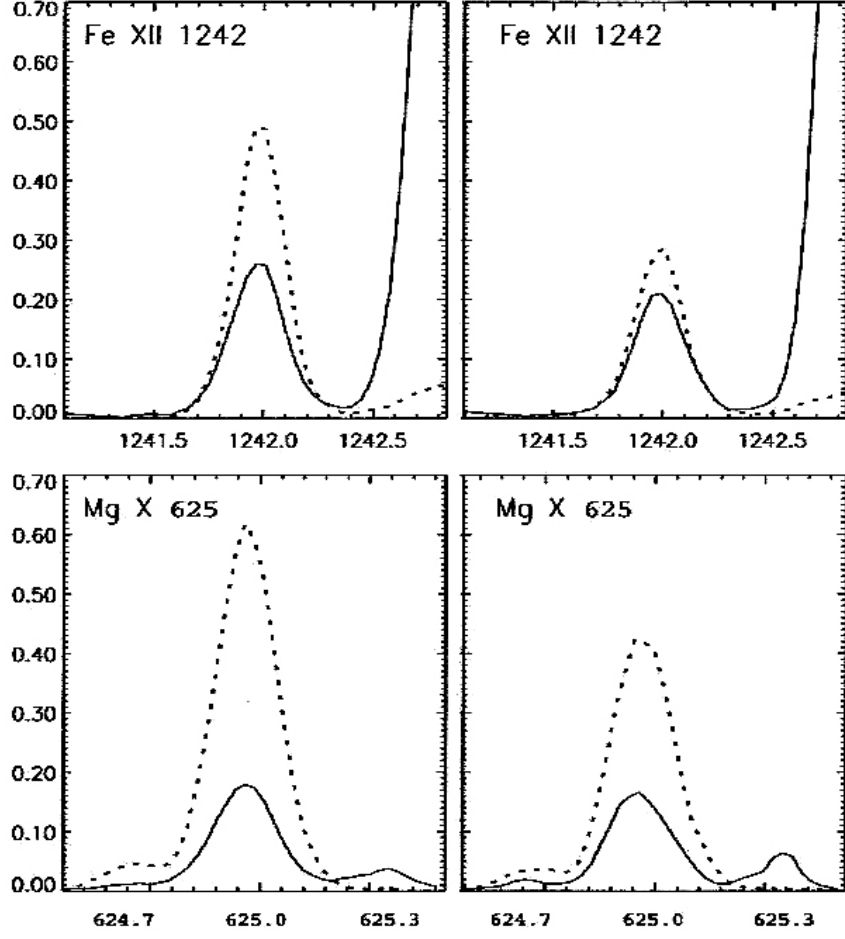


Figure 10. Emission profiles of two coronal lines in the prominence free background (*dashes*) and in the prominences (*full lines*) E/70N (*left panels*) and E/42N (*right panels*), showing the absorption of Fe XII 1241.95 Å by the cool prominence material, and the additional absorption by the Lyman continuum of Mg X 624.95 Å.

3.4. Widths of the EUV lines

The widths of even our narrowest observed Lyman lines $\Delta\lambda_e^{Ly}/\lambda \approx 14 \cdot 10^{-5}$ largely exceed the Doppler widths $[\Delta\lambda_D/\lambda]_H = 4.3 \cdot 10^{-5}$ expected for the broadening parameters $T_{kin} = 8500$ K and $V_{nth} = 5$ km/s obtained from the ground-based spectra (Sec. 2.3). The observed widths of the Lyman lines are closer to those of the 'hot' rather than of the 'cool' (chromospheric) EUV lines in Figures 11 and 12. This may be a further hint that the Lyman lines are emitted in prominence layers which are in contact with the hot corona (cf., above).

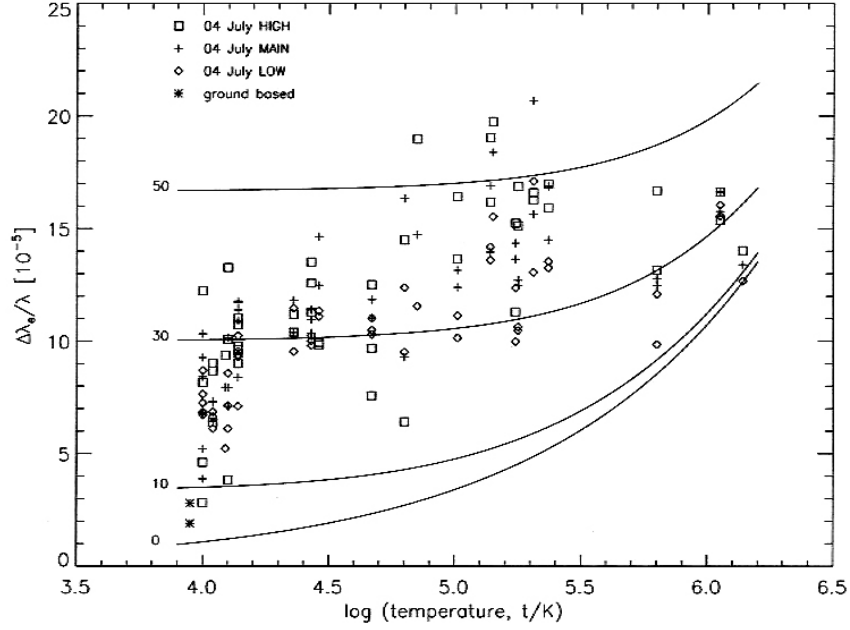


Figure 11. EUV line widths at 1/e intensity versus the formation temperature for the three spatial locations within prominence E/70N: the widths of the ground-based spectra of Ca II 8542 Å and He I 10830 Å are also plotted (asterisks); for comparison Doppler widths calculated for the non-thermal velocities 0, 10, 30, 50 km/s and the (abscissa) temperatures with $\mu_{atom} = 16$ (oxygen) are shown .

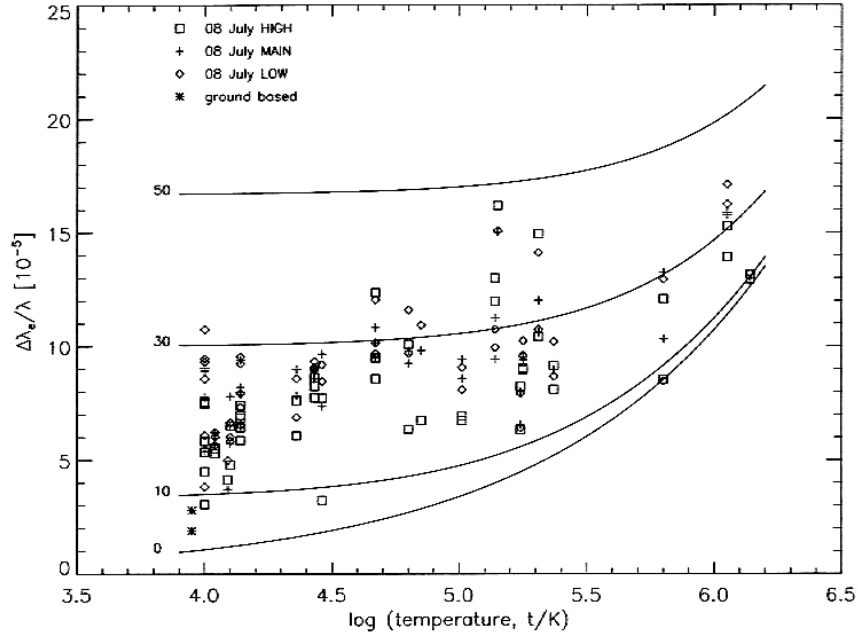


Figure 12. Same as Figure 11 but for prominence E/42N .

3.4.1. Correction of narrow lines for the SUMER profile

For the observed narrow EUV lines from neutrals and singly charged atoms (i.e., 'chromospheric lines'), the standard correction for the instrumental profile of detector A (cf., Wilhelm et al., 1997) yields reduced line widths $7 \cdot 10^{-5} < \Delta\lambda_e/\lambda < 12 \cdot 10^{-5}$ for prominence E/70N and $5 \cdot 10^{-5} < \Delta\lambda_e/\lambda < 10 \cdot 10^{-5}$ for prominence E/42N. If we apply the revised correction with broader instrumental profiles by Chae, Schühle, and Lemaire (1998), the resulting widths $5 \cdot 10^{-5} < \Delta\lambda_e/\lambda < 9 \cdot 10^{-5}$ are still significantly broader than those obtained by Mariska, Doschek, and Feldman (1979) from observations with the NRL slit spectrograph on *Skylab* (at a spectral resolution of 60 mÅ). Interestingly, their reduced widths of lines from neutral and singly charged atoms of typically $\Delta\lambda_e/\lambda \approx 3 \cdot 10^{-5}$ are very near to those of our Ca IR line (entered in Figs. 11 and 12).

We verified that the excess widths even in the maximum de-convoluted spectra from SUMER can not originate from our spatial averaging: the ground-based spectra do not yield sensibly wider profiles when equally averaged over 7 arcsec. The small dispersion of macro-shifts $< |5|$ km/s (cf., Fig. 2) can not produce such a significant additional line broadening via spatial averaging. *We thus consider the observed narrow widths of EUV lines from neutral and singly charged atoms to be still affected by a underestimated instrumental profile of the SUMER spectrograph*, and conclude that we cannot draw definite conclusions from these widths of 'chromospheric' EUV lines.

3.4.2. The broader 'hot' lines

Almost insensitive to instrumental broadening are the wider lines from ions in higher charged states (C III, C IV, S III S IV etc.), corresponding to formation temperatures $T_{form} > 10^{4.8}$ K (cf., Figs. 11 and 12). Their widths smoothly increase with T_{form} . We consider this increase to be real, since Mariska, Doschek, and Feldman (1979) found comparable widths $\Delta\lambda_e/\lambda = 8 \cdot 10^{-5}$ and a similar increase with T_{form} , which they interpreted as a discontinuity of the non-thermal velocities between cool and hot emitting material. This increase of line widths is particularly pronounced in prominence E/70N (Fig. 11) at location 'HIGH' where lines from higher-charged ions are enhanced (cf., Fig. 8). At that location, the ground-based spectra show marked macro-shifts and a 'fuzzy' structure.

In order to give a reference for line broadening by temperature and by non-thermal velocities, v_{nth} , we add in Figures 11 and 12 curves of calculated Doppler widths as a function of the temperature (abscissa) for various values of v_{nth} , assuming the atomic mass of oxygen ($\mu = 16$). We see a marked difference between the two prominences: the emissions from higher charged ions give for prominence E/70N systematically larger v_{nth} than for E/42N.

TABLE I
 Radiances [$\text{mW sr}^{-1} \text{m}^{-2}$] FWHM [\AA] (second row) in the 7'' averages
 'LOW', 'MAIN', and 'HIGH' (Figures 13 and 14) for prominences E/70N and E/42N.

Ion	λ [\AA]	$\log T$	70 – L	70 – M	70 – H	42 – L	42 – M	42 – H
Cont (Ly)	912–13	4.20	34.74	26.38	8.761	38.05	31.02	25.27
H I Ly19	914.29	4.20	6.576	5.816	2.516	8.748	5.425	4.594
			0.211	0.232	0.222	0.217	0.207	0.168
H I Ly18	914.58	4.20	6.054	5.306	2.303	7.989	6.101	4.273
			0.224	0.224	0.161	0.193	0.215	0.202
H I Ly17	914.92	4.20	6.647	6.445	2.647	9.911	6.066	4.677
			0.222	0.219	0.181	0.216	0.220	0.198
H I Ly16	915.33	4.20	7.692	6.683	3.668	9.864	6.696	4.416
			0.264	0.248	0.234	0.226	0.217	0.175
H I Ly14	916.43	4.20	8.960	7.548	2.887	11.96	7.633	5.410
			0.276	0.292	0.236	0.226	0.267	0.229
H I Ly13	917.18	4.20	9.143	8.155	4.146	10.16	7.299	5.179
			0.258	0.274	0.247	0.216	0.210	0.230
H I Ly12	918.13	4.20	10.22	7.967	3.634	13.26	8.054	6.673
			0.293	0.284	0.261	0.261	0.267	0.229
H I Ly11	919.35	4.20	11.18	8.765	4.227	12.35	8.578	6.016
			0.307	0.293	0.239	0.263	0.275	0.218
H I Ly10	920.97	4.20	10.78	9.440	4.154	12.12	9.784	5.908
			0.297	0.296	0.261	0.252	0.265	0.224
H I Ly9	923.15	4.20	16.87	14.38	6.009	15.71	13.05	7.688
			0.373	0.355	0.334	0.293	0.323	0.261
H I Ly8	926.23	4.20	18.11	16.37	6.908	18.00	14.19	8.810
			0.372	0.323	0.301	0.282	0.321	0.272
H I Ly7	930.75	4.20	24.97	21.89	8.956	23.32	18.96	12.04
			0.425	0.367	0.343	0.353	0.393	0.324
H I Ly6	937.80	4.20	39.69	34.22	14.12	36.75	31.71	19.50
			0.483	0.435	0.392	0.422	0.384	0.354
H I Ly5	949.74	4.20	79.60	63.98	25.94	69.06	62.74	31.67
			0.548	0.486	0.456	0.453	0.473	0.412
Si I	1256.49	4.00	1.142	0.624	0.219	0.878	0.678	0.727
			0.182	0.194	0.256	0.198	0.162	0.122
S I	1316.54	4.00	0.620	0.420	0.277	0.320	0.218	0.260
			0.159	0.149	0.179	0.188	0.171	0.164
N I	1318.98	4.00	0.835	0.660	0.254	0.789	0.562	0.403
			0.168	0.185	0.062	0.134	0.122	0.099
C I	1313.46	4.00	0.344	0.160	0.160	0.269	0.265	0.173
			0.147	0.114	0.101	0.235	0.198	0.117
C I	1315.92	4.00	0.358	0.200	–	0.116	0.201	0.119
			0.150	0.085	–	0.084	0.118	0.067

Figure 12.

TABLE I
Continued.

Ion	λ [Å]	$\log T$	$70 - L$	$70 - M$	$70 - H$	$42 - L$	$42 - M$	$42 - H$
O I	1302.17	4.04	179.2	107.5	32.11	253.3	185.3	142.7
			0.144	0.159	0.188	0.135	0.135	0.119
O I	1304.86	4.04	180.6	91.29	32.14	219.4	173.9	139.0
			0.149	0.158	0.196	0.131	0.130	0.120
O I	1306.03	4.04	144.2	78.66	19.86	180.3	125.5	104.9
			0.133	0.140	0.139	0.123	0.125	0.115
Fe II	1563.79	4.09	27.93	22.58	13.47	31.86	26.38	15.37
			0.136	0.207	0.244	0.130	0.097	0.108
Ni II	1317.22	4.10	2.863	1.881	0.572	3.839	2.856	1.551
			0.134	0.174	0.221	0.132	0.126	0.105
S II	1253.80	4.10	4.086	3.118	1.219	4.969	3.753	2.243
			0.179	0.212	0.277	0.139	0.136	0.136
Si II	1260.44	4.14	20.90	19.40	9.977	27.08	20.35	10.78
			0.215	0.246	0.202	0.194	0.168	0.135
Si II	1264.74	4.14	42.24	43.97	24.43	62.36	52.28	26.74
			0.201	0.248	0.226	0.201	0.198	0.156
Si II	1309.28	4.14	16.33	13.14	6.037	21.74	16.69	10.29
			0.155	0.183	0.213	0.143	0.140	0.128
C II	1334.53	4.36	465.0	347.4	138.0	489.9	407.6	257.8
			0.212	0.231	0.231	0.153	0.174	0.135
C II	1335.71	4.36	711.2	501.7	203.8	647.6	543.1	379.4
			0.255	0.263	0.249	0.191	0.200	0.169
N II	1083.99	4.43	10.42	8.027	1.991	11.31	8.306	4.723
			0.177	0.187	0.227	0.164	0.161	0.156
N II	1084.58	4.43	21.65	17.06	5.276	20.41	16.77	9.667
			0.185	0.198	0.244	0.163	0.164	0.149
N II	1085.71	4.43	41.59	33.56	9.535	44.84	32.64	20.07
			0.181	0.206	0.204	0.169	0.155	0.140
Si III	1298.96	4.46	8.857	11.75	–	14.50	5.711	1.034
			0.240	0.270	–	0.183	0.209	0.070
Si III	1312.59	4.46	1.510	1.503	0.273	2.135	0.740	0.170
			0.248	0.320	0.215	0.201	0.161	0.169
He II	927.85	4.67	1.649	1.017	0.170	2.341	1.840	0.763
			0.162	0.183	0.117	0.157	0.157	0.191
He II	942.51	4.67	3.863	2.344	0.337	4.667	2.940	1.184
			0.173	0.173	0.152	0.189	0.170	0.149
He II	1084.94	4.67	41.87	30.99	6.186	54.96	36.15	11.72
			0.186	0.199	0.226	0.175	0.172	0.155
S III	1077.14	4.80	2.702	2.460	1.087	2.683	1.491	0.231
			0.222	0.293	0.260	0.174	0.166	0.181

Figure 12.

TABLE I
Continued.

Ion	λ [Å]	$\log T$	$70 - L$	$70 - M$	$70 - H$	$42 - L$	$42 - M$	$42 - H$
Si IV	1066.65	4.80	1.312	0.658	0.156	1.440	1.352	0.249
			0.169	0.165	0.114	0.206	0.174	0.113
C III	1247.41	4.85	2.555	2.018	0.675	2.327	1.487	0.407
			0.240	0.306	0.394	0.227	0.204	0.140
C IV	1548.21	5.01	797.2	669.1	220.1	713.8	496.2	149.2
			0.287	0.339	0.352	0.234	0.243	0.179
C IV	1550.77	5.01	292.5	251.3	82.65	272.5	195.5	59.98
			0.262	0.320	0.424	0.209	0.222	0.174
S IV	1062.66	5.14	4.014	3.676	1.679	5.403	2.256	0.481
			0.251	0.247	0.337	0.176	0.167	0.230
S IV	1072.99	5.14	6.515	5.976	2.499	8.923	3.567	0.646
			0.243	0.302	0.289	0.192	0.201	0.214
N IV	924.28	5.15	3.922	2.981	0.858	3.376	2.549	0.818
			0.239	0.283	0.304	0.232	0.231	0.249
S V	786.49	5.24	17.77	28.24	9.754	7.524	1.414	1.309
			0.162	0.188	0.148	0.084	0.086	0.083
O IV	787.73	5.24	33.24	49.04	21.80	11.15	2.687	3.817
			0.131	0.179	0.200	0.104	0.105	0.108
N V	1238.82	5.25	167.1	103.4	28.23	106.3	77.01	20.02
			0.216	0.257	0.348	0.198	0.194	0.185
N V	1242.80	5.25	79.01	53.65	14.27	55.03	38.46	9.772
			0.220	0.263	0.313	0.212	0.197	0.187
S VI	933.40	5.31	22.70	14.29	4.789	21.49	13.91	3.770
			0.203	0.243	0.253	0.167	0.165	0.162
S VI	944.55	5.31	16.43	11.04	2.927	13.33	7.049	2.142
			0.269	0.325	0.261	0.222	0.189	0.235
O V	629.77	5.37	328.3	385.5	171.2	62.41	52.12	50.00
			0.139	0.177	0.178	0.107	0.094	0.096
Ne VIII	770.43	5.80	39.95	41.06	31.00	23.11	17.08	14.73
			0.155	0.164	0.214	0.166	0.170	0.155
Mg X	624.95	6.05	26.63	35.59	55.82	45.32	32.98	23.09
			0.167	0.164	0.160	0.178	0.164	0.145
Fe XII	1241.95	6.14	13.74	11.81	10.21	12.09	9.226	5.780
			0.262	0.277	0.290	0.273	0.264	0.272

Figure 12.

4. Conclusions

The straightforward 'classic' determination of the plasma parameters kinetic temperature, T_{kin} , and non-thermal (Maxwellian) velocity, v_{nth} , by comparison of line-widths from atoms with different mass and in same excitation state was not possible for the EUV emissions from atoms in lower excitation states (chromospheric lines), since the instrumental profile of the SUMER spectrograph is too broad and not precisely enough defined for those narrow prominence lines.

The He II 1084 Å components (even though still affected by the SUMER instrumental profile) are so narrow that the He II formation has to be assumed close to that of the 'chromospheric' lines from neutrals and singly ionized atoms. This is also supported by the spatial similarity of the line radiances (Figs. 8 and 9).

A comprehensive set of higher Lyman lines ($5 \leq k \leq 19$) yields relative widths $(\Delta\lambda_e/\lambda)^{Ly} > 14 \cdot 10^{-5}$ which smoothly increase with line strength (i.e., with optical thickness). Even their smallest widths largely exceed $\Delta\lambda_e/\lambda = 4.3 \cdot 10^{-5}$ calculated for H I lines with $T_{kin} = 8500$ K and $v_{nth} = 5$ km/s from ground-based spectra. The well-defined emission relation of the Lyman lines (curve-of-growth) suggests a common state of excitation; their behavior significantly differs from that of the lines of the Balmer, Paschen, Brackett, and Pfund series, which typically yield $T_{kin} = 6000$ K a value, which would require for the observed widths of the Lyman lines non-thermal velocities $v_{nth} > 30$ km/s.

The spatial resolution, though not matching that of the ground-based observations, allows us to distinguish regions with enhanced emissions of neutral and singly charged ions (mainly associated with 'cool' regions) from those of 'hotter' regions with enhanced emissions of lines from higher charged atoms (such as O IV, O V, N V, S V, S VI). This indicates that hotter locations exist separately from a cooler and denser main prominence region, as is qualitatively indicated from the two-dimensional images in Figure 1. All Lyman lines show a similar spatial variation, and do not noticeably weaken at locations where lines from highly charged ions are strengthened. This finding and the large widths of the Lyman lines suggest that their emissions will also originate from hot regions.

The 'discontinuity' between the widths of cool ('chromospheric') lines and those from highly charged atoms (cf., Figs. 11 and 12) indicates different dynamical states of the emitting plasma, where not only the temperature but also the non-thermal broadening is increased. This does principally not allow us to distinguish between separate regions with 'hotter' and, respectively, 'cooler' emission or 'hot' transition regions surrounding 'cool' cores of each prominence thread. For a final decision between the various models, space and ground-based spectra should spatially resolve the prominence threads.

Acknowledgements We appreciate numerous discussions with W. Curdt, E. Marsch, and K. Wilhelm, and support from the Max-Planck-Institut für Aeronomie, Katlenburg-Lindau; we thank an unknown referee for helpful suggestions. A. Garcia (IAP) and B. Bovelet (Göttingen) kindly performed some of the graphics. The Gregory Coudé telescope on Tenerife is operated by the Universitäts-Sternwarte, Göttingen (USG). and the Vacuum Tower Telescope by the Kiepenheuer Institut für Sonnenphysik, Freiburg (KIS) at the Spanish 'Observatorio del Teide' of the Instituto de Astrofísica de Canarias. The SUMER project is financially supported by the 'Deutsche Agentur für Raumfahrt-Angelegenheiten' (DARA), the 'Centre National d'études Spaciales (CNES), and the 'European Space Administration' (ESA).

References

- Chae, J., Schühle, U., and Lemaire, P.: 1998, *Astrophys. J.* **505**, 957.
- Dammasch, I./E., Stellmacher, G. and Wiehr, E.: 2003, *Solar Phys.* **217**, 133.
- de Boer, C. R., Stellmacher, G., and Wiehr, E.: 1998, *Astron. Astrophys.* **334**, 280.
- Engvold O.: 1978, *Solar Phys.* **56**, 87.
- Heinzel, P., Schmieder, B., Vial, J.-C. and Kotrc, P.: 2001, *Astron. Astrophys.* **370**, 281.
- Hirayama, T.: 1971, *Solar Phys.* **17**, 50.
- Mariska, J. T., Doschek, G. A. and Feldman, U.: 1979, *Astron. Astrophys.* **232**, 929.
- Stellmacher, G. and Wiehr, E.: 1994, *Astron. Astrophys.* **286**, 302.
- Stellmacher, G. and Wiehr, E.: 1995, *Astron. Astrophys.* **299**, 921.
- Stellmacher, G. and Wiehr, E.: 2000, *Solar Phys.* **196**, 357.
- Wijk, J. E., Dere, K. and Schmieder, B.: 1993, *Astron. Astrophys.* **273**, 267.
- Wilhelm, K. et al.: 1997, *Solar Phys.* **170**, 75.
- Yang, C. Y., Nicholski, R. W., and Morgan, F. J.: 1975, *Solar Phys.* **5**, 351.